Atom probe tomography of space-weathered lunar ilmenite grain surfaces

Jennika GREER [1,2]*, Surya. S. ROUT[2,6], Dieter ISHEIM[3,4], David N. SEIDMAN[3,4],
Rainer WIELER[5], and Philipp R. HECK [1,2]

[1]Department of the Geophysical Sciences, The University of Chicago, Chicago, Illinois 60637, USA
[2]Robert A. Pritzker Center for Meteoritics and Polar Studies, Field Museum of Natural History, Chicago, Illinois 60605, USA
[3]Northwestern Center for Atom Probe Tomography (NUCAPT), Northwestern University, Evanston, Illinois 60208, USA
[4]Department of Materials Science and Engineering, Northwestern University, Evanston, Illinois 60208, USA
[5]Institute of Geochemistry and Petrology, ETH Zürich, Zürich, Switzerland
[6]Present address: Electron Microscopy Unit, Hamburg University of Technology, 21073 Hamburg, Germany
*Corresponding author. E-mail: jennika@uchicago.edu

Abstract–The surfaces of airless bodies, such as the Moon and asteroids, are subject to space weathering, which alters the mineralogy of the upper tens of nanometers of grain surfaces. Atom probe tomography (APT) has the appropriate 3-D spatial resolution and analytical sensitivity to investigate such features at the nanometer scale. Here, we demonstrate that APT can be successfully used to characterize the composition and texture of space weathering products in ilmenite from Apollo 17 sample 71501 at near-atomic resolution. Two of the studied nanotips sampled the top surface of the space-weathered grain, while another nanotip sampled the ilmenite at about 50 nm below the surface. These nanotips contain small nanophase Fe particles (~3 to 10 nm diameter), with these particles becoming less frequent with depth. One of the nanotips contains a sequence of space weathering products, compositional zoning, and a void space (~15 nm in diameter) which we interpret as a vesicle generated by solar wind irradiation. No noble gases were detected in this vesicle, although there is evidence for ^{4}He elsewhere in the nanotip. This lunar soil grain exhibits the same space weathering features that have been well documented in transmission electron microscope studies of lunar and Itokawa asteroidal regolith grains.

INTRODUCTION

Space weathering is the alteration of the upper surface of materials on airless bodies due to the simultaneous effects of irradiation by cosmic and solar rays, electromagnetic radiation, and impacts from micrometeorites. These interactions cause physical and chemical alteration of the surface, impact vaporization, and ion sputtering and implantation, which lead to gardening and change in optical properties of the surface materials (Hapke 2001; Chapman 2004; Bennett et al. 2013; Pieters and Noble 2016). Products of space weathering include agglutinates, redeposition rims, Britt-Pieters particles/microphase metallic iron (>40 nm; mpFe; Lucey and Noble 2008), nanophase metallic iron (<40 nm; npFe; Hapke 2001; Lucey and Noble 2008), and vesicles filled with implanted solar wind. Due to these npFe and mpFe particles, space-weathered materials have reddened and darkened spectra relative to pristine samples in visible and near-IR, and a blue slope in shorter wavelengths (UV; Noble et al. 2001; Hendrix and Vilas 2006; Starukhina and Shkuratov 2011; Pieters and Noble 2016; Raut et al. 2018).

The abundance of these products produced by space weathering depends on the composition of the soil grain (Zhang and Keller 2011; Burgess and Stroud 2018) as well as an object's distance from the Sun and the length of time it has been exposed to the weathering environment (Zhang and Keller 2011; Pieters and Noble 2016). Redeposition rims are thin layers on the outside of the grain that are compositionally distinct from the host grain and can have inclusions like npFe (Pieters and Noble 2016). Study of material from the surface of the Moon and asteroid Itokawa shows the presence of a

single amorphous layer or complex rims, sometimes with gas-filled vesicles, on the surface of the studied grains (Keller and McKay 1997; Noguchi et al. 2014). The npFe particles present in these rims on lunar and Itokawa soil grains (e.g., inclusion-rich and complex rims on the lunar particles and redeposition and partially amorphous rims on Itokawa particles) formed through a combination of deposition of the vapor produced during micrometeorite impact, deposition of elements sputtered by solar wind, and thermal reduction during micrometeorite impact melting (Moroz et al. 1996; Keller and McKay 1997; Noguchi et al. 2014; Pieters and Noble 2016). The total depth of these rims can be up to 200 nm thick (Keller and McKay 1997), and it can be difficult to differentiate the contributions from micrometeorite impacts from those of the solar wind ions in the formation of the rims. However, work by Zhang and Keller (2011) shows that micrometeorite impacts are a dominant contributor to the deposition rims on lunar soil grains during the initial stages of space weathering. Solar wind ions have a speed range of ~300 to 800 km s^{-1} (Reisenfeld et al. 2013), and are implanted up to about 200 nm deep into solid matter with a concentration maximum at about 30–50 nm (e.g., Heber et al. 2014). Solar wind–implanted H could play a role in the development of npFe within agglutinate glasses and formation of vesiculated rims on lunar and Itokawa soil grains (McKay et al. 1991; Keller and McKay 1997; Pieters and Noble 2016).

Transmission electron microscope (TEM) studies of naturally and artificially space-weathered materials have led to better understanding of the formation process of the rims around space-weathered grains, but there are still some open questions that need to be investigated at near atomic spatial resolution, including (1) what is the depth concentration profile, at high spatial resolution, of implanted H, OH, and noble gases within the space-weathered rims; (2) what is the concentration of noble gases within vesicles in space-weathered rims; and (3) what is the composition of different elements within multilayered space-weathered rims. The new generations of probe-corrected scanning transmission electron microscopes equipped with electron energy loss spectroscope and atom probe tomography (APT) have the required spatial resolution to try to answer the above questions.

Ilmenite (FeTiO$_3$) is an opaque oxide mineral that is a common accessory phase in terrestrial igneous and metamorphic rocks (Deer et al. 1992) and can comprise up to about 20% of lunar soils (e.g., Papike et al. 1991). Ilmenite has been proposed as a building resource for a future lunar base, specifically as a source of Fe, Ti, O, and solar wind–implanted H (O'Neill et al. 1977; McKay and Williams 1979; Papike et al. 1991). However, as a soil accumulates more and more

agglutinates with increasing exposure to the space environment, the soil becomes harder to utilize as a resource (McKay and Williams 1979), making it necessary to better understand space weathering processes. Elements other than Mg that are commonly found in terrestrial ilmenite (e.g., Cr, Mn, Al) are typically present only at minor or trace levels in lunar samples (Papike et al. 1991). Ilmenite is more retentive to solar wind–implanted He and Ne than plagioclase and other minerals (Signer et al. 1977), and is therefore a prime target to study implanted noble gases.

The noble gas composition of ilmenite in lunar soil has been well studied, as the isotopic composition of the noble gases can provide an unambiguous signature of the soil's interaction with the solar wind. Noble gas mass spectrometry coupled with extraction through both stepwise heating and acid etching suggested that the noble gases were located in the outermost grain layers (Benkert et al. 1993). TEM work with electron energy loss spectroscopy has shown that the helium present in the outermost rims of these grains is concentrated in vesicles and planar defects (Burgess and Stroud 2018).

Atom probe tomography is an analytical imaging technique that is increasingly being used for geo- and cosmochemistry (e.g., Heck et al. 2014; Valley et al. 2014, 2015; Parman et al. 2015; Lewis et al. 2015; Peterman et al. 2016; Daly et al. 2017; Rout et al. 2017). APT is a technique complementary to TEM, in that it generates quantitative 3-D information with atom-by-atom distribution of elements, at a higher resolution for compositional data. In APT, atoms are field evaporated from the surface of a sample and detected by a position-sensitive time-of-flight mass spectrometer. This way, both the local compositions and spatial distributions can be determined in three dimensions (Seidman and Stiller 2009; Blum et al. 2017). With APT, a sample volume of typically 100 nm in diameter can be analyzed at near atomic spatial resolution, which makes it ideal to study the nanoscale features formed by space weathering. Here, we present the first APT study from a naturally space-weathered sample.

SAMPLES AND METHODS

Lunar Dust Sample

Atom probe nanotips were prepared from a single ilmenite grain from Apollo 17 sample 71501, aliquot 284, separated for ilmenite grains 150–200 μm in diameter. Soil 71501 has been classified as submature (Heiken and McKay 1974). It is composed of mainly basalt fragments and basalt minerals. Ilmenite comprises 8% modal content of the soil in the 90–
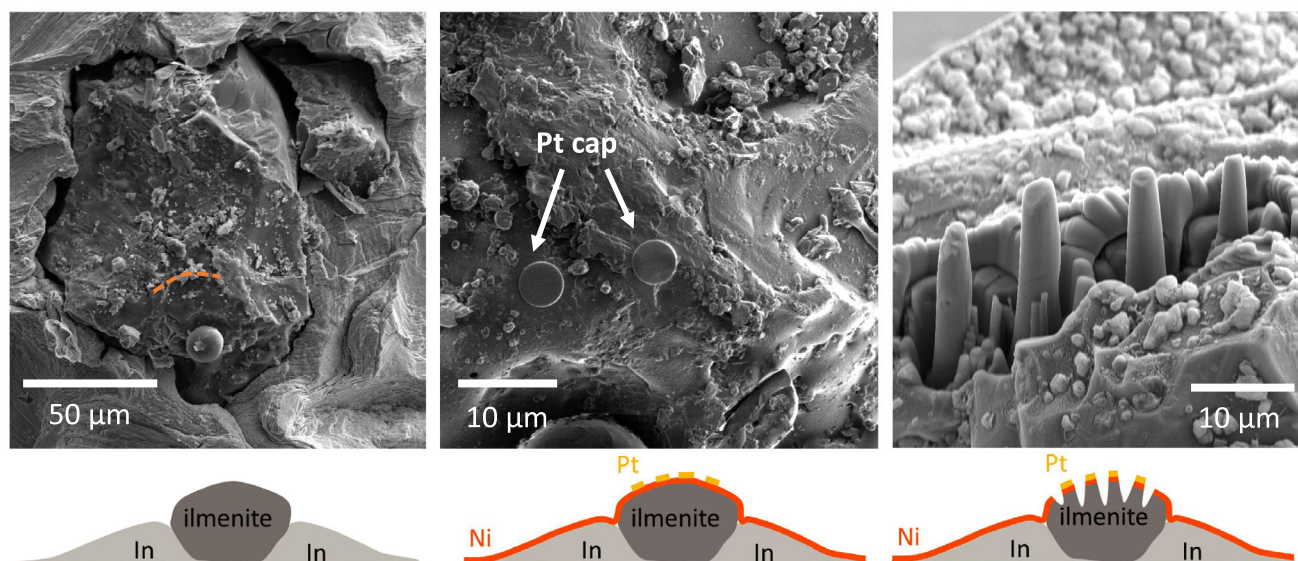
Fig. 1. SEM images and drawings of grain and sample preparation for APT. A) Ilmenite is hand-picked and pressed into indium mounted on an SEM stub. The orange dashed line indicates the location of the grain ridge and represents a topographic high from where samples were extracted. B) The grain is ion beam sputter-coated with Ni and protective caps of Pt are deposited in the FIB with the Pt precursor gas injection system (GIS), and then (C) milled with annuli to produce spokes that will be lifted out. (Color figure can be viewed at wileyonlinelibrary.com.)

150 μm range. This sample has been of great interest particularly due to its high solar wind content (e.g., Hintenberger et al. 1974; Signer et al. 1977; Frick et al. 1988; Benkert et al. 1993).

Sample Preparation

We selected a single grain with a diameter of about 130 μm from an ilmenite separate that had been prepared by hand picking from a grain-size separate obtained by sieving under ethanol (Benkert et al. 1993). The ilmenite separate and single grains thereof had been previously extensively studied for noble gas concentrations and isotopic compositions (e.g., Benkert et al. 1993; Wieler et al. 1996). These studies showed that essentially all grains from this sample contain solar wind–implanted noble gases.

The grain used for this study was pressed into indium on an SEM Al stub mount (Fig. 1a). Some of this In was then pressed over the edges of the grain to secure it. The grain's composition was analyzed qualitatively with SEM-EDS to confirm that it was ilmenite. The sample was ion-beam-sputter coated with Ni to protect the mineral surface from Ga^+ ion irradiation during focused-ion beam (FIB)-based sample preparation (Fig. 1b).

FIB Microscopy

To prepare samples for APT, we used the TESCAN LYRA3 FIB-SEM at the University of Chicago equipped with a Ga liquid-metal ion source, an Oxford Instruments micromanipulator, and an Oxford Instruments gas injection system (GIS). Circular platinum caps 2 μm in diameter were deposited on top of the region of interest using ion beam–assisted deposition for 5–10 min to further protect the sample during milling (Fig. 1b). This deposition was done with a low current (<10 pA) to minimize ion-beam implantation. The grain had no flat surfaces suitable for milling out a lamella as is done with traditional APT sample preparation (e.g., Rout et al. 2017). To reduce the milling required to produce a liftout, and to facilitate the liftout process, a topographic ridge of this grain was annularly milled with the FIB to produce several spokes 1–2 μm in diameter (Fig. 1c), which were then lifted out using a micromanipulator. These spokes were then mounted onto flat-top Si micro tips (provided by Cameca Instruments) by GIS Pt deposition. The spokes were shaped with the FIB following traditional APT sample preparation steps (e.g., Larson et al. 1999). The sample shaping started with a 10 kV, 35 pA beam. The sides of each sample were milled on both sides of the tip, rotated 90°, and then milled on the remaining two sides. This resulted in a truncated pyramid-shaped tip approximately 0.5 μm wide at the top. The tips were annularly milled from the top with a 10 kV, 15 pA beam to a radius of 0.2 μm, which rounds the tip out to a conical shape. At this point, any secondary tips (sharp points outside the annulus unintentionally created during sample preparation) were removed so that the

primary tip stood alone for 5 μm. A low-energy mask with a 5 kV, 30 pA beam sharpened the tips to a final radius, ranging between 50 and 20 nm, and removed surface contamination. During milling, the sample was monitored with an in-beam backscatter electron detector, and the milling was stopped when the bright cap of platinum on the tip disappeared in the image. One of the nanotips (Tip D, discussed below), had surficial material removed so that deeper, unaltered material could be analyzed.

Atom Probe Tomography

The nanotips were analyzed with a LEAP 4000X Si atom probe tomograph at the NUCAPT facility of Northwestern University. The atom probe was run in laser mode with a UV laser (355 nm wavelength), with a pulse repetition rate of 250 kHz, a pulse energy of 35–50 pJ, and a temperature of 30 K, conditions suitable for electrically nonconductive materials. A total of four nanotips were produced for this analysis. Tip A was manually stopped at 5 M atoms. This nanotip did not yield useful data, as only coating materials were analyzed (see Table 2). Tip B was analyzed in two sessions. The first session analyzed coating materials, and after ~30 min of evaporation, the target material (ilmenite) was reached. The session was manually stopped, and analysis continued with only ilmenite present. Tip B fractured after 12.5 M atoms were counted. The analysis of Tip C was manually stopped at 16 M atoms, after the Fe present was no longer in nanophase form. Analysis of Tip D was manually stopped at 10 M atoms as enough atoms in the region of interest had been counted. The maximum voltage that was reached was 7 kV.

We have previously shown that APT can be used as a standardless analytical technique (Rout et al. 2017), since all elements have approximately the same detection efficiency. The samples described here were measured with the LEAP 4000X Si, with ~50% detection efficiency (e.g., Seidman and Stiller 2009; Kelly and Lawson 2012). A potential instrumental bias with detector dead time from C isotopes in diamond was found in previous work (Heck et al. 2014); this is caused by counting deficiencies due to highly correlated field evaporation and field evaporation of molecular ions in combination with detector dead-time limitations (Stephan et al. 2015). This combination of effects is particularly pronounced in materials that have irregular field evaporation behavior, such as diamond, or for elements with a single dominant isotope. For such samples, isotope data need to be corrected for by using a statistical method as described by Stephan et al. (2015). For most other materials with more uniform field evaporation behavior and multiple isotopes, such as the samples studied here, such a correction is very small and thus can be ignored (Rout et al. 2017).

Data were reduced using the Cameca IVAS computer code, a commercial APT data analysis software. The elemental and molecular ion species that have been detected and identified in the mass spectrum are provided in Table 1, and the spectra for these samples with labeled peaks are shown in Fig. 2. Species with peaks overlapping with isobaric interferences (listed in Table 1) were identified based on their natural solar system isotopic abundances. The automatic background correction from IVAS was applied to the mass spectrum. Molecular ions and both singly and doubly charged species were included in the 3-D reconstructions (Figs. 3 and 4) and elemental concentrations. Nanotip geometry of the reconstruction was approximated using the half apex angle of the conical tip (also known as the shank angle) determined in SEM images. Subsets of the data were analyzed in selected spherical and cylindrical regions of interest (ROI). Concentration profiles were generated along the z-axis of the nanotip from binned cylindrical ROIs.

Isobaric peak overlaps prevented the identification of some rare species. Singly charged ^{20}Ne has a peak at a mass-to-charge-state ratio of 20 u, but is obscured by the much larger $(^{40}$Ca$)^+$ and $(^{26}$Mg^{16}O$)^{++}$ peaks at the same location in the mass spectrum (Table 1). The mass resolving power of the APT is generally insufficient to separate isotopic and molecular isobar peaks.

For comparisons to published data, the APT data were converted from atom% to oxide wt%.

RESULTS

Overview

Of four nanotips that were produced from this grain, three yielded useful data—Tips B, C, and D (Fig. 3 and Material S1 in supporting information; analysis of Tip A showed only coating materials, Table 2). Tip B was extracted from the outermost surface of the grain. The suite includes the redeposition rim; nanophase and microphase Fe ranging from 5 to >30 nm in diameter; and a section near the base of the nanotip that is more homogenous in the distribution of elements, particularly Fe, than the above layers (Fig. 3). During analysis of Tip B, the first atoms came from coating materials that were on top of this tip (not present in this reconstruction but preserved on a separate analysis that is not shown here). Tip C contains more

Table 1. List of identified peaks and possible isobaric overlaps.

| Mass to charge state	Assigned species	Possible isobaric overlaps	Mass to charge state	Assigned species	Possible isobaric overlaps	Mass to charge state	Assigned species	Possible isobaric overlaps
1	$^{1}H+$		27	$^{54}Fe++$	$^{27}Al+$	58	$^{58}Fe+$	
2	$(^{1}H_2)+$	$^{2}H+$	27.5	$^{55}Mn++$		60	$(^{28}Si^{16}O_2)+$	
3	$(^{1}H_3)+$	$^{3}He+$	28	$^{56}Fe++$	$^{28}Si+$	61	$(^{29}Si^{16}O_2)+$	
9	$(^{1}H_2{}^{16}O)++$		28.5	$^{57}Fe++$		62	$(^{46}Ti^{16}O)+$	$(^{30}Si^{16}O_2)+$
12	$^{24}Mg++$	$^{12}C+$	29	$^{58}Fe++$	$^{29}Si+$	63	$(^{47}Ti^{16}O)+$	
12.5	$^{25}Mg++$		31	$(^{46}Ti^{16}O)++$		64	$(^{48}Ti^{16}O)+$	
13	$^{26}Mg++$	$^{13}C+$	31.5	$(^{47}Ti^{16}O)++$		65	$(^{49}Ti^{16}O)+$	
13.5	$^{27}Al++$		32	$(^{48}Ti^{16}O)++$	$^{32}S+,\ ^{16}O_2+$	66	$(^{50}Ti^{16}O)+$	
16	$^{16}O+$		32.5	$(^{49}Ti^{16}O)++$		70	$(^{54}Fe^{16}O)+$	
17	$(^{16}O^{1}H)+$	$^{17}O+$	33	$(^{50}Ti^{16}O)++$		71	$(^{55}Mn^{16}O)+$	
18	$(^{1}H_2{}^{16}O)+$	$^{18}O+$	40	$^{40}Ca+$	$^{40}Ar+,\ (^{24}Mg^{16}O)++$	72	$(^{56}Fe^{16}O)+$	
20	$(^{40}Ca)+$	$^{20}Ne+,\ (^{24}Mg^{16}O)++$	43	$(^{54}Fe^{16}O_2)++$		73	$(^{57}Fe^{16}O)+$	
22	$(^{28}Si^{16}O)++$		44	$(^{56}Fe^{16}O_2)++$	$(^{28}Si^{16}O)+$	74	$(^{58}Fe^{16}O)+$	
23	$^{46}Ti++$		44.5	$(^{57}Fe^{16}O_2)++$	$(^{29}Si^{16}O)+$	78	$(^{46}Ti^{16}O_2)+$	
23.5	$^{47}Ti++$		45	$(^{58}Fe^{16}O_2)++$	$(^{30}Si^{16}O)+$	79	$(^{47}Ti^{16}O_2)+$	
24	$^{48}Ti++$	$^{24}Mg+$	54	$^{54}Fe+$		80	$(^{48}Ti^{16}O_2)+$	
24.5	$^{49}Ti++$		56	$^{56}Fe+$		81	$(^{49}Ti^{16}O_2)+$	
25	$^{50}Ti++$	$^{25}Mg+$	57	$^{57}Fe+$		82	$(^{50}Ti^{16}O_2)+$	
26	$^{52}Cr++$	$^{26}Mg+$	57.5	$^{115}In++$				
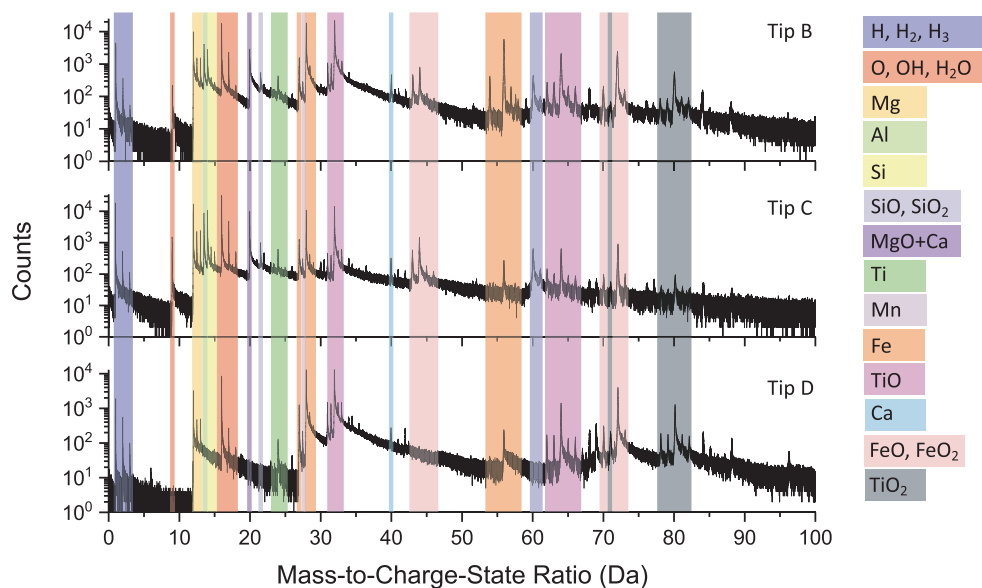
Fig. 2. APT mass spectra of tips B, C, and D, before background correction. Identified peaks are labeled with colored stripes and can include both singly and doubly charged species. (Color figure can be viewed at wileyonlinelibrary.com.)

npFe particles than Tip B, and these particles are all small, ranging from 2 to 10 nm in diameter (Fig. 2), with no mpFe present. After these two nanotips were analyzed, Tip D was re-sharpened to expose more of the unaltered part of the grain. Although it still contains npFe in the top 40 nm, much of the nanotip has a homogenous distribution of Fe (Fig. 2).

Zoning

The presence of space weathering features and differences in elemental composition allow us to distinguish three different zones with depth, similar to features described by Keller and McKay (1997), Noguchi et al. (2014), and Burgess and Stroud (2018).
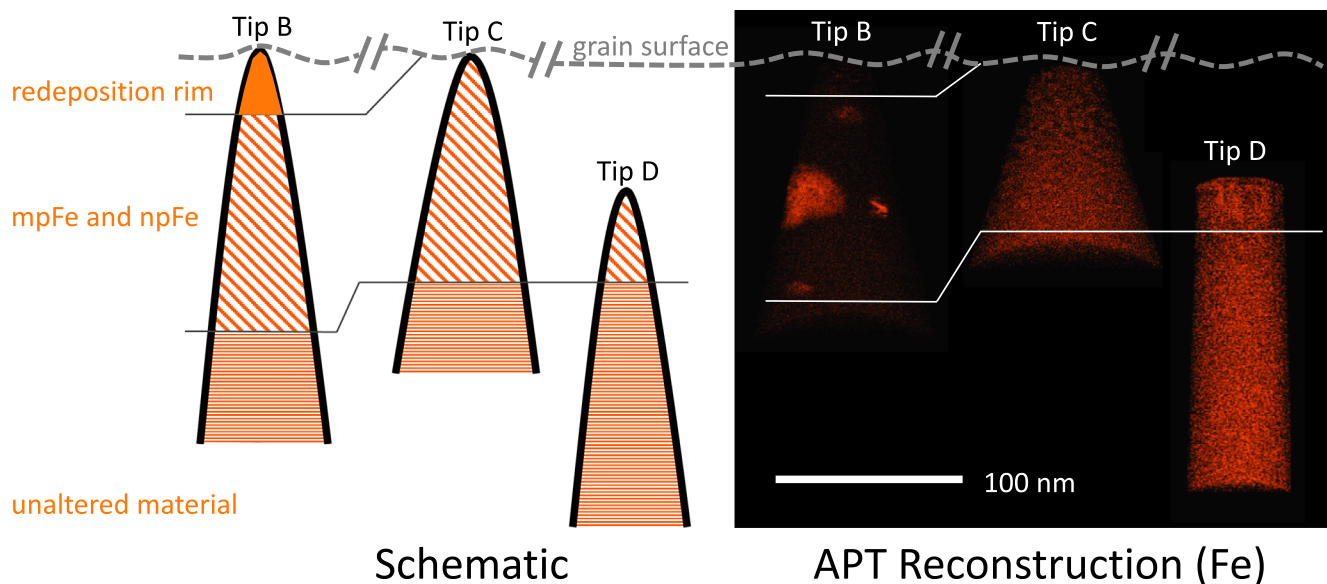
Fig. 3. A "stratigraphic correlation-like" illustration of analyzed tips next to reconstructions of APT data, with only Fe atoms shown. The different zones are marked by thin gray lines. All three tips contain strikingly different features—the Fe atoms, represented by orange points in the right half of the figure, are distributed very differently from nanotip to nanotip. This is to be expected with Tip D, which was sampled from deeper in the grain, but Tip B and Tip C are both within approximately 10 nm of the surface. Distances are not to scale. (Color figure can be viewed at wileyonlinelibrary.com.)

Redeposition Rim

The redeposition rim was present in the reconstruction of Tip B. This rim is about 15 nm thick. Fe is heterogeneously distributed in both $(Fe)^{+,++}$ and $(FeO)^{+,++}$ as npFe particles ranging from 2 to 5 nm. Trace elements like Si, Mg, Ca, and Al are enriched in the rim (Figs. 4 and 5).

Micro- and Nanophase Fe

The heterogeneity in the distribution of Fe is different in nanotips B and C. Tip C has a relatively homogenous distribution of Fe particles. These particles have a size of 2–10 nm, and as with the nanoparticles in the redeposition rim of Tip B, are correlated with $(FeO)^{+,++}$. In Tip B, there are no npFe particles below the redeposition rim. Instead, this section, approximately 110 nm thick, is dominated by a large mpFe particle, 30 nm in diameter (cutoff in the analysis, most likely >30 nm in total), and is not as enriched in Si, Mg, Ca, and Al as the redeposition rim (Fig. 5). These particles are pure $(Fe)^{+,++}$, with $(FeO)^{+,++}$ only present within their rims. These $(FeO)^{+,++}$ rims are also slightly enriched in $(TiO)^{+}$ and $(MgO)^{+}$ relative to the rest of the sample. The entire zone is depleted in elemental Ti relative to other sections of the nanotip (Fig. 4). This zone contains a void space approximately 20 nm in diameter.

Unaltered Material

Below the section of the nanotip containing large Fe particles in Tip B, and below the nanophase Fe particle-rich zone in Tips C and D, is material that contains no detected products of space weathering. All of the analyzed species are distributed homogenously throughout this zone, including Fe. Cr is more abundant in this zone than elsewhere (Fig. 4).

Implanted Solar Wind

Tip B contains a void space, with a short axis of 8 nm and a long axis of 14 nm, which could either be a vesicle or a bubble that was formed due to implantation-generated defects (e.g., Linez et al. 2013) or escaping volatiles during the production and deposition of a melt or vapor splash. We interpret it as a vesicle similar to those described in Burgess and Stroud 2018. This is because we detect 3 ± 2 $(^{4}He)^{+}$ atoms (1σ) above background at the same depth and in close proximity to the vesicle (Fig. S1 in supporting information). This $(^{4}He)^{+}$ detection seems to be due to the opening of the vesicle at the apex of the sample nanotip during analysis.

The solar wind ion implantation profiles are best represented by Tip C. The profile of H species present in Tip C is consistent with H implantation (Fig. 6), not a tail-off that would be indicative of adsorbed residual
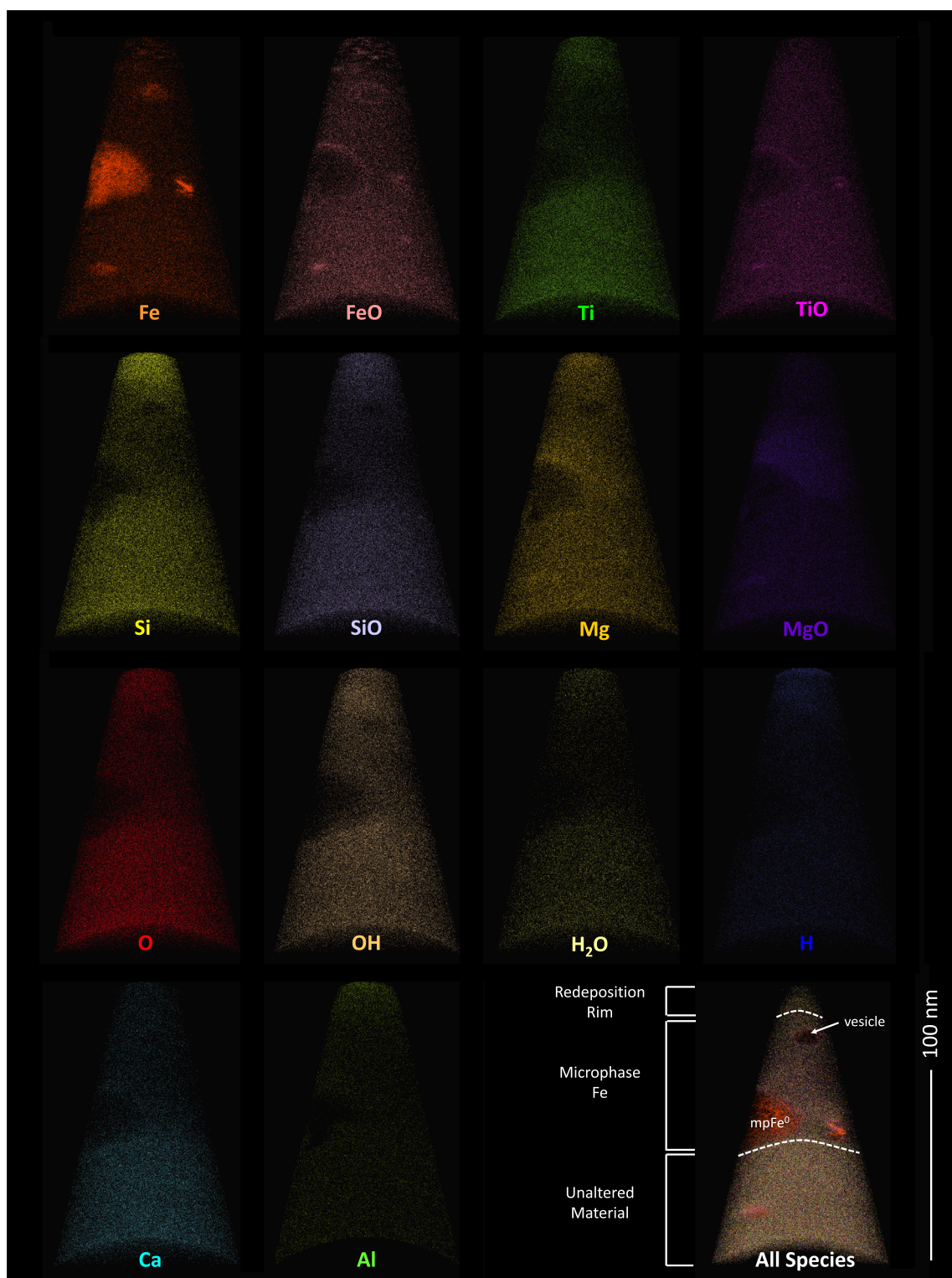
Fig. 4. Reconstructions of Tip B in different atomic and molecular species, showing the heterogeneity of Fe when concentrated in nanophase particles, the higher concentration of species like Si and H near the top of the tip, and the absence of other species in the large, pure microphase Fe particle. The reconstruction in the lower right shows a cross section reconstruction of all identified species, exposing the vesicle. The vesicle is surrounded by an Fe-rich rim. (Color figure can be viewed at wileyonlinelibrary.com.)

Table 2. Summary of tips analyzed.

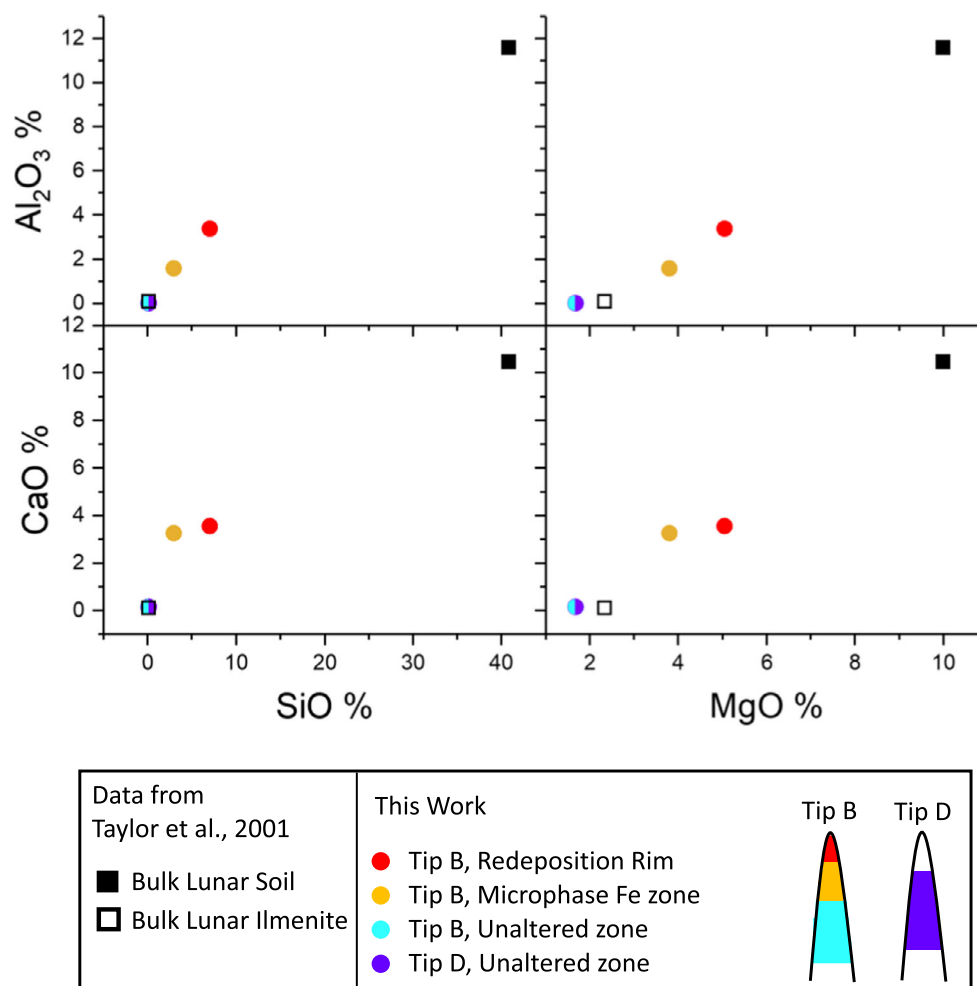|	No. atoms detected (M)	Reconstruction tip length (nm)	Reconstruction tip base diameter (nm)	Short description
A	6	–	—	Coating materials
B	16	140	80	Redeposition rim
C	12.5	110	100	Nanophase Fe particles
D	10	170	50	Unaltered material

Fig. 5. Minor and trace element compositions of selected regions within tips B and D compared to data from Taylor et al. (2001). In these diagrams, APT atomic% data were converted to oxide wt%. 1σ error bars are within the point for these data, and were not reported in Taylor et al. (2001). (Color figure can be viewed at wileyonlinelibrary.com.)

H in the atom probe chamber, as in Tip B (Fig. S2 in supporting information). The greatest concentration of H occurs at a depth of 40–50 nm, consistent with H^+ implantation at typical energies (Ziegler et al. 2012). H-bearing molecular ions, like OH^+ and H_2O^+, are also present (Fig. 4); the H in these molecular ions is also sourced from the solar wind (i.e., Ichimura et al. 2012; Liu et al. 2012).

No Ne was unambiguously detected in any of the nanotips nor their ROIs. The peak at mass-to-charge

(m/z) state 20 corresponds to $(Ca)^{++}$, the molecular ion $(MgO)^{2+}$, as well as $^{20}Ne^+$, and these isobaric overlaps overwhelm any signal from $^{20}Ne^+$ that could be present. The $m/z = 20$ peak correlates with $(TiO)^+$, $(TiO)^{2+}$, and $(FeO)^+$ peaks, and therefore, the signal is likely to be dominated by Ca and MgO, not Ne. $(MgO)^{2+}$ is distributed heterogeneously throughout the nanotip, correlating to npFe and the microphase Fe particles. If the $m/z = 20$ species was mostly $^{20}Ne^+$, it would be expected to occur at discrete locations such as
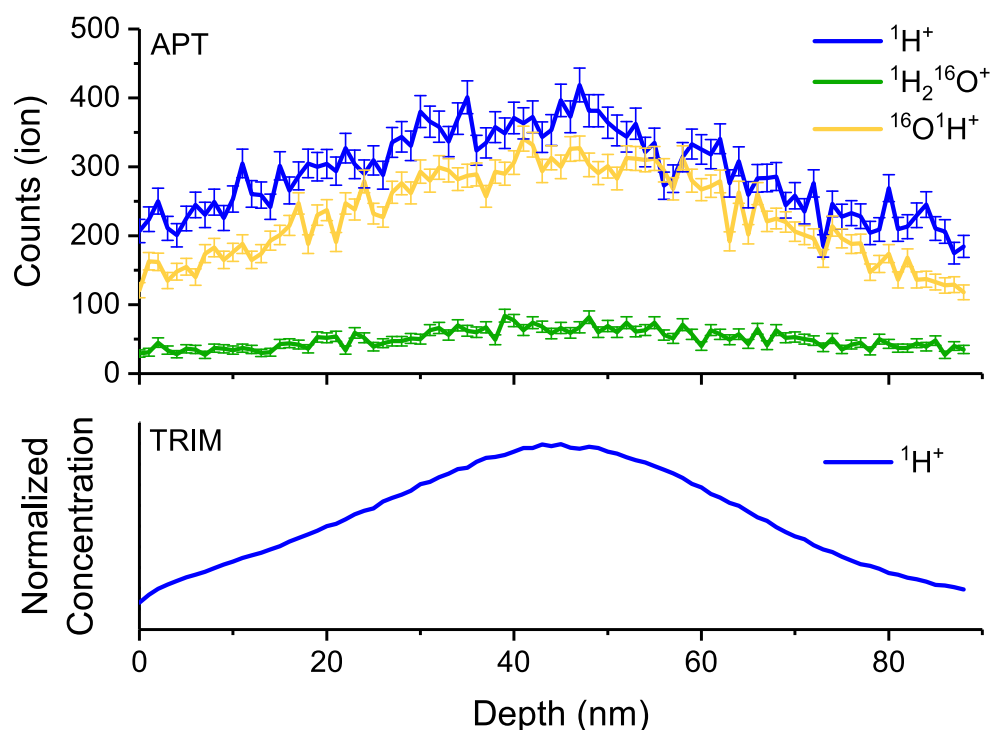
Fig. 6. Concentration profile in Tip C of selected H-bearing species. The H-bearing species H^+ and OH^+ clearly show a concentration peak at a depth of 40–50 nm, with a shape consistent with H implantation at 4 keV into a $FeTiO_3$ glass with a density of 4.75 g cm^{-3} as simulated by SRIM/TRIM (Ziegler et al. 2012). Surface-adsorbed H usually present in large quantities on the top of the tip is not present in this reconstruction. (Color figure can be viewed at wileyonlinelibrary.com.)

within the vesicle and within other defects, similar to the solar wind He (Burgess and Stroud 2018). The species at a mass-to-charge-state ratio 40 does not correlate with $(MgO)^{2+}$ and is interpreted as $^{40}Ca^+$. The species at 22 is interpreted as $(Si^{28}O^{16})^{2+}$, and since the Si enrichment is in the outermost section of the nanotip (the same region we would expect Ne enrichment), and is much more abundant than Ne, ^{22}Ne could not be identified in the integrated data set of each nanotip. Any heavier noble gases were below our detection limit.

DISCUSSION

Comparison of Different Sample Tips

Lateral variability in products of micrometeorite impact melting on the nanometer and centimeter scale has been seen on lunar samples (Christoffersen et al. 1996; Noble et al. 2013). The characteristics of the sample nanotips vary greatly (Fig. 3), though they were all extracted from a small surface area with dimensions of 5×25 μm on the same grain. Tips B and C were prepared using the same method. While none of the capping materials were measured on Tip C, the top of

the nanotip is no more than 10 nm below the surface of the grain, as determined from careful monitoring of the nanotip during milling. Although this may be enough to remove a thin redeposition rim, the distribution of Fe between the different nanotips is still very different. Tip D was milled to expose a deeper part of the grain and, since most of the nanotip does not have npFe, is a more representative sample of unweathered grain material. The different distribution of space weathering products between B and C is due to the sample nanotip's original position in the grain, as the nanotips come from different locations on the grain's ridge, and therefore could have been exposed to different events. These results show the heterogeneous nature of space weathering on different regions of identical composition on even a single grain.

Two elemental concentration profiles, comprising a cylinder the length of the sample, were generated for Tip B. One of the Fe concentration profiles was generated to include most of the nanotip material, including the mpFe particle. There is a significant spike in Fe between 60 and 80 nm from a concentration of about 20 atom% to a maximum of 60 atom% (Fig. S2). A profile in the same nanotip that does not include as much material but avoids all of the large particles

shows a slight decrease in Fe concentration at the same depth as the largest particle. This suggests that the Fe in the particle is intrinsic to the samples, as Fe is depleted in the region immediately surrounding the microphase particle. In Tip C, which has no large mpFe particles, the concentration of Fe remains constant with depth. Tips B, C, and D were extracted from locations on the grain that were less than 25 μm apart, which illustrates the heterogeneity on the micro- as well as nanoscale.

Comparison with Other Space-Weathered Samples

Here, we analyze our samples within the framework that was developed by Noguchi et al. (2014). These authors defined three zones (I–III) that described the different types of space weathering modification found in grains from the asteroid Itokawa. The zones we observe in the lunar material have the same compositional characteristics as the Noguchi et al. (2014) zones but have different depth ranges. By using these zones, lunar and asteroidal space weathering effects can be directly compared, even for large differences in the duration of space exposure.

Zone I, composed of products from redeposition, is present on Tip B. However, in Itokawa particles, the redeposition rim is thinner (~5 nm) than that of our sample (~20 nm). The regolith of Itokawa is thought to be younger than the lunar regolith sampled by Apollo 17 as asteroidal regoliths have a shorter lifetime, due to the lower gravity compared to the Moon (Miyamoto et al. 2006; Nagao et al. 2011). Previous TEM studies of lunar ilmenite also show that this topmost layer (1) is Si-rich and ranges from 10 to 50 nm thick and (2) has a high concentration of npFe and vapor-deposited species like Ca, Al, Mg, and S (Christoffersen et al. 1996; Noble et al. 2006; Zhang and Keller 2010).

Zone II, dubbed the partially amorphized zone in Noguchi et al. (2014), corresponds to the area of Tip B that is dominated by the microphase Fe particle (see Fig. 5, yellow zone). The thickness of the npFe-bearing rim in Tip C is about 60 nm, which is comparable to the nanocrystalline and disordered rim described on lunar ilmenites (Christoffersen et al. 1996; Burgess and Stroud 2018) and only 10–20 nm thicker than that of Itokawa olivine grains (Noguchi et al. 2011). The npFe particles are 2–5 nm in diameter, larger than those typically seen in Itokawa grains (Noguchi et al. 2014). The npFe particles in this zone range in size from 2 to >30 nm (2–5 nm in Tip C and 2–30 nm in Tip B) and this is similar to the range (10–50 nm) seen within the disordered rim of the ilmenite studied by Burgess and Stroud and Zhang and Keller (2010). We do not see nanophase sulfides. There is an isobaric overlap between $^{32}S^+$ and $(TiO)^{2+}$ (Table 1), but the species at $m/z = 32$ does not correlate with the nanophase particles and is therefore dominated by $(TiO)^{2+}$. We also do not see any TiO_2 precipitates within this region as seen by Christoffersen et al. (1996) and Burgess and Stroud (2018). While asteroids and the Moon do not experience the same space weathering environments, this shows that the process responsible for producing the npFe must be active on asteroids as well as the Moon, or that different processes result in the same behavior in different materials.

Elemental compositions of Zones I and II in our samples (Fig. 5) fall between the two endmember compositions of bulk lunar soil and bulk lunar ilmenite (Taylor et al. 2001). The latter corresponds to the unaltered zones (see text below).

Zone III, the unaltered or crystalline zone, is present in both the base of Tips B and C, and most of Tip D (see Fig. 5, green and purple zones). This area is homogenous and has a minor and trace element composition almost identical to bulk lunar ilmenite (Fig. 5; Taylor et al. 2001). The MgO, CaO, and Al_2O_3 compositions of this zone in Tips B and D are nearly identical (MgO = $1.68 \pm 0.55\%$ for both nanotips, CaO = $0.15 \pm 0.19\%$ for both, and $Al_2O_3 = 0.02 \pm 0.13\%$ for Tip B and $0.01 \pm 0.06\%$ for Tip D).

Although the Noguchi et al. (2014) zone classification can be applied well to Tip B, this classification does not necessarily accurately describe the other nanotips studied here or other lunar samples, which may have other products that were not seen in our samples (Keller and McKay 1997). Zone II is similar to the outer rim described by Burgess and Stroud (2018), which has 10–50 nm Fe particles in a disordered matrix. The Itokawa samples do not contain the larger mpFe particles observed here, which are located in the section of Tip B that corresponds to Zone II. However, Tip B contains a vesicle with a size that is more comparable to the Itokawa grains (20–50 nm) than those found in other lunar regolith soil grains (100–200 nm; Noguchi et al. 2014). Previous TEM studies show that the npFe is sometimes elongated parallel to the surface of the host ilmenite grain, which is the orientation we see in our samples (Zhang and Keller 2010).

Redeposition Rim Mixing

An advantage of APT is its high spatial resolution, which allows for compositional analysis of small volumes not resolvable with other techniques. When converted to oxide wt%, some of the minor elements plot on a mixing line (Fig. 5) between the bulk lunar ilmenite and the bulk lunar soil as measured by Taylor

et al. (2001). Generally, the unaltered material (Noguchi Zone III) is identical within error to bulk lunar ilmenite. In some cases, the unaltered material has smaller concentrations of these minor and trace elements, as the bulk ilmenite measurements may have included the space-weathered rim and are thus more enriched in elements like Mg and Al. The redeposition rim is distinguished from the rest of the nanotip by its different composition (Fig. 4). The redeposition rim is more enriched in the minor elements than the nanophase Fe area, suggesting that some of the rim material is sourced from outside of the ilmenite grain and is a true redeposition rim, and the different composition is not due to just the preferential removal of Fe and O. We are unable to determine if this microstructure was altered by irradiation.

Previous TEM studies of ilmenite grains (Bernatowicz et al. 1994; Christoffersen et al. 1996; Noble et al. 2006; Zhang and Keller 2010; Burgess and Stroud 2018) from the lunar soil also show the presence of a redeposition rim on the grain surfaces that is enriched in Mg, Al, Si, and Ca. Since most of these elements are not present, or only present in minor amounts in ilmenite, this leads to the conclusion that they were formed by condensation of vapor produced by the impact of micrometeorites on adjacent (non-ilmenite) grains and by deposition of materials sputtered by energetic solar wind ions from the nearby grains. Although several studies have suggested that micrometeorite impacts are the dominant contributor to the deposition rims, Bernatowicz et al. (1994) suggested that solar wind radiation damage could also contribute to their formation.

Hydrogen and Noble Gases

Hydrogen is more abundant than He and Ne in the solar wind by factors of about 25 and 17,000 times, respectively (Wieler 2002). We do not see these expected ratios in our samples. In Tip C, where the H profile is indicative of solar wind implantation, the concentration (from the "unaltered" volume used for Fig. 5; purple) is 6.2×10^{20} H atoms cm^{-3}, and the fluence (irradiation over a surface area) is 6.9×10^{18} H atoms cm^{-2} (including atoms from H hydride compounds observed in the mass spectrum). In Tip B, the hotspot of ^{4}He, which shows three ^{4}He atoms above background (3 ± 2 ^{4}He atoms above background [1σ]; Fig. S1), is observed in a location near the edge of the vesicle, which suggests that these atoms were evaporated when the vesicle was first opened during sample preparation with the FIB or field evaporation with APT.

We can attempt to estimate the expected ^{4}He amount present in our nanotips by (1) normalizing the noble gas concentration measured in other ilmenite grains from sample 71015 to the nanotip's volume and (2) dividing the measured H concentration in the tip by the H/He ratio in the solar wind (Wieler 2002). With the first method, we estimate the number of ^{4}He atoms present in the volume of Tip B (3.7×10^{-16} cm^3) based on the ^{4}He concentrations measured in ilmenite separates from sample 71501 by Benkert et al. (1993). This is a very conservative estimate assuming that the entirety of the grains analyzed by Benkert et al. (1993) has the same solar wind He concentration as the nanotip representing mostly the outermost (solar wind–bearing) region of a grain. An expected count brings the estimate to ~4800 ^{4}He atoms in the entirety of Tip B. The measured ^{4}He concentration of the entirety of Tip B, 3 atoms, is only ~0.5‰ of the expected concentration of ^{4}He. In the second method, the surface-adsorbed H dominates the signal in Tip B, so we use the bulk H concentration of Tip C to estimate the expected amounts in Tip B. Assuming the ^{4}He concentration is homogeneous throughout the entire nanotip, we obtain an estimate of ~7800 ^{4}He atoms in the entirety of Tip B. This is within a factor of 1.6 of the estimate based on the first method. If there was no ^{4}He migration into the vesicle, ~20–30 ^{4}He atoms would be expected in a volume the size of the vesicle in Tip B (2.5×10^{-18} cm^3). However, given that the solar wind He was likely concentrated in the vesicle, it is possible that all of the ^{4}He from this nanotip was lost upon opening (either during sample preparation or analysis) before it could be analyzed.

We did not detect any Ne, although both the lower limits for ^{20}Ne and ^{22}Ne concentrations based on single grain analyses from Benkert et al. (1993) were above our detection limit in the spectrum of the vesicle (Fig. 7). Using the H/Ne ratio from Wieler (2002), ~11 ^{20}Ne atoms are expected to be present in Tip B. Other species, like ^{3}He and ^{21}Ne, are not detectable above background in such an analysis, but are detectable if concentrated in a small volume, such as a vesicle. Even though there is an isobaric overlap between ^{20}Ne, ^{40}Ca^{++}, and $(^{24}Mg^{16}O)^{++}$, an increased concentration of a species with a mass-to-charge state of 20 that correlates with either other noble gases or a vesicle is likely to be ^{20}Ne, as Mg is present in the 1–7 wt% level but is only in the sample material, not the void space. ^{36}Ar is present in too low abundances to be expected to be present in a sample nanotip of this volume.

Burgess and Stroud (2018) showed that the He present in the grain rims is concentrated in these vesicles and in planar defects, and vesicles develop due the interaction between the soil particle and the solar wind. There could be several explanations or a combination
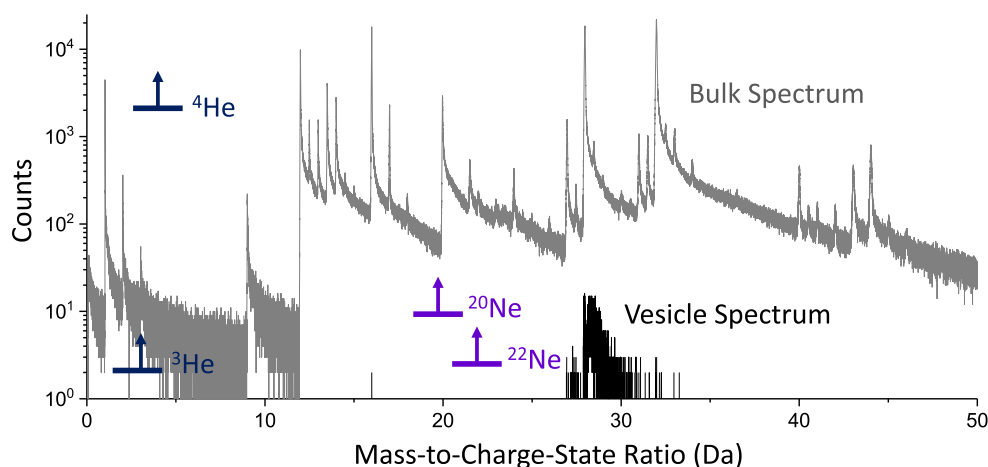
Fig. 7. The gray spectrum shows the integrated composition of Tip B. The black spectrum shows the composition of a spherical ROI centered on the void space in Tip B. Some of the signal comes from the material immediately surrounding the vesicle, which was included due to the oblate nature of the vesicle. Lower limits on noble gas concentration for He and Ne based on bulk data (calculated as describe the main text) are shown. (Color figure can be viewed at wileyonlinelibrary.com.)

thereof for a lower-than-expected concentration of He and the non-detection of Ne, including (1) the electric field was not high enough to quantitatively ionize He and Ne, which escaped to vacuum as neutrals; (2) after the vesicle was opened during APT analysis, most of the He and Ne escaped without having been ionized; (3) the sample was clipped during FIB milling for sample preparation and the majority of the gas escaped at this time. Although He in this form is a difficult element to measure with APT, due to the difficulty in controlling field evaporation and field ionization of gaseous He in a vesicle, there have been multiple studies that have detected He in metals (e.g., Wagner and Seidman 1979; Seidman et al. 1980; Edmondson et al. 2013), and this remains an open area of study for cosmochemical materials.

SUMMARY AND CONCLUSIONS

We successfully used APT to characterize space weathering products in lunar ilmenite.

- In our samples, we see a redeposition rim, iron clusters (both a microphase Fe particle and nanophase Fe particles), and a vesicle that likely once held solar wind.
- We observe compositional heterogeneity in ilmenite at the nanoscale, the micron scale, and on different surfaces of the same grain. This implies small-scale intragrain variability of exposure to space weathering.
- In Tip C, H-bearing species are present in the greatest amounts at a depth range of 40–50 nm, fully consistent with solar wind implantation.

- In a vesicle at 30 nm depth below the surface 3 ± 2 [4]He atoms were detected. While this is significantly below the concentration expected (only 0.1% of the expected value), this is likely due to the difficulty of quantitatively ionizing He before it is lost to the sample chamber.
- We have shown that APT can be successfully used for targeted cosmochemical, tomographic analyses of space-weathered samples while keeping total sample consumption very low.

We conclude that APT is an ideal analytical method to study surface effects of precious samples, such as mission-returned samples like those presented here.

and Energy (ISEN) at Northwestern University. We appreciate the constructive reviews by Katharine Burgess and Michelle Thompson, and thank associate editor Carlé M. Pieters.

Editorial Handling—Dr. Carlé Pieters

REFERENCES

Benkert J., Baur H., Signer P., and Wieler R. 1993. He, Ne, and Ar from the solar wind and solar energetic particles in lunar ilmenites and pyroxenes. *Journal of Geophysical Research* 98:13147.

Bennett C., Pirim C., and Orlando T. M. 2013. Space-weathering of solar system bodies: A laboratory perspective. *Chemical Reviews* 113:9086–9150.

Bernatowicz T. J., Nichols, R. H. Jr. and Hohenberg C. M. 1994. Origin of amorphous rims on lunar soil grains (abstract). 25th Lunar and Planetary Science Conference. pp. 105–106.

Blum T. B., Darling J. R., Kelly T. F., Larson D. J., Moser D. E., Perez-Huerta A., Prosa T. J., Reddy S. M., Reinhard D. A., and Saxey D. W. 2017. Best practices for reporting atom probe analysis of geological materials. In *Microstructural geochronology: Planetary records down to atom scale*, edited by Moser D. E., Corfu F., Darling J. R., Reddy S. M. and Tait K. Hoboken, NJ: Wiley. pp. 369–373.

Burgess K. D. and Stroud R. M. 2018. Phase-dependent space weathering effects and spectroscopic identification of retained helium in a lunar soil grain. *Geochimica et Cosmochimica Acta* 224:64–79.

Chapman C. R. 2004. Space weathering of asteroid surfaces. *Annual Review of Earth and Planetary Sciences* 32:539–567.

Christoffersen R., McKay D. S., and Keller L. P. 1996. Microstructure, chemistry, and origin of grain rims on ilmenite from the lunar soil finest fraction. *Meteoritics & Planetary Science* 31:835–848.

Daly L., Bland P. A., Saxey D. W., Reddy S. M., Fougerouse D., Rickard W. D. A., and Forman L. V. 2017. Nebula sulfidation and evidence for migration of free floating refractory metal nuggets revealed by atom probe microscopy. *Geology* 45:847–850.

Deer W. A., Howie R. A., and Zussman J. 1992. *An introduction to rock forming minerals*, 2nd ed. Harlow, UK: Longman Scientific & Technical.

Edmondson P. D., Parish C. M., Zhang Y., Hallén A., and Miller M. K. 2013. Helium distributions in a nanostructured ferritic alloy. *Journal of Nuclear Materials* 434:210–216.

Frick U., Becker R. H., and Pepin R. O. 1988. Solar wind record in the lunar regolith—Nitrogen and noble gases. Proceedings, 18th Lunar and Planetary Science Conference. pp. 87–120.

Hapke B. 2001. Space weathering from Mercury to the asteroid belt. *Journal of Geophysical Research* 106:10,039–10073.

Heber V. S., McKeegan K. D., Burnett D. S., Duprat J., Guan Y., Jurewicz A. J. G., Olinder C. T., and Smith S. P. 2014. Accurate analysis of shallowly implanted solar wind ions by SIMS backside depth profiling. *Chemical Geology* 390:61–73.

Heck P. R., Stadermann F. J., Isheim D., Auciello O., Daulton T. L., Davis A. M., and Elam J. W. 2014. Atom-probe analyses of nanodiamonds from allende. *Meteoritics & Planetary Science* 49:453–467.

Heiken G. and McKay D. S. 1974. Petrography of Apollo 17 soils. Proceedings, 5th Lunar Conference. pp. 843–860.

Hendrix A. R. and Vilas F. 2006. The effects of space weathering at UV wavelengths: S-class asteroids. *The Astronomical Journal* 132:1396–1404.

Hintenberger H., Weber H. W., and Schultz L. 1974. Solar, spallogenic, and radiogenic rare gases in Apollo 17 soils, and breccias. Proceedings, 5th Lunar Science Conference. pp. 2005–2022.

Ichimura A. S., Zent A. P., Quinn R. C., Sanchez M. R., and Taylor L. A. 2012. Hydroxyl (OH) production on airless bodies: evidence from H+/D+ ion-beam experiments. *Earth and Planetary Science Letters* 345–348:90–94.

Keller L. P. and McKay D. S. 1997. The nature and origin of rims on lunar soil grains. *Geochimica et Cosmochimica Acta* 61:2311–2341.

Kelly T. F. and Lawson D. J. 2012. Atom probe tomography 2012. *Annual Review of Materials Research* 42:1–31.

Larson D. J., Foord D. T., Petford-Long A. K., Liew H., Blamire M. G., Cerezo A., and Smith G. D. W. 1999. Field-ion specimen preparation using focused ion-beam milling. *Ultramicroscopy* 79:287–293.

Lewis J. B., Isheim D., Floss C., and Seidman D. N. 2015. $^{12}C/^{13}C$-ratio determination in nanodiamonds by atom-probe tomography. *Ultramicroscopy* 159:248–254.

Linez F., Gilabert E., Debelle A., Desgardin P., and Barthe M.-F. 2013. Helium interaction with vacancy-type defects created in silicon carbide single crystal. *Journal of Nuclear Materials* 436:150–157.

Liu Y., Guan Y., Zhang Y., Rossman G. R., Eiler J. M., and Taylor L. A. 2012. Direct measurement of hydroxyl in the lunar regolith, and the origin of lunar surface water. *Geoscience Nature* 5:779–782.

Lucey P. G. and Noble S. K. 2008. Experimental test of a radiative transfer model of the optical effects of space weathering. *Icarus* 197:348–353.

McKay D. S. and Williams R. J. 1979. A geologic assessment of potential lunar ores. In *Space resources and space settlements*, edited by Billingham J., Gilbreath W., and O'Leary B. Washington, D.C.: NASA ARC. pp. 243–255.

McKay D. S., Heiken G., Basu A., Blanford G., Simon S., Reedy R., French B. M., and Papike J. 1991. The lunar regolith. In *Lunar sourcebook*, edited by Heinken G. H., Vaniman D. T., and French B. M. Cambridge, UK: Cambridge University Press. pp. 285–356.

Miyamoto H., Yano H., Scheeres D., Sasaki S., Barnouin-Jha O., Gaskell R. W., Cheng A., Demura H., Fujiwara A., Hashimoto T., Hirata N., Honda C., Ishiguro M., Kubota T., Michikami T., Nakamura A. M., Nakamura R., Saito J., and Yokota Y., and Hayabusa Team. 2006. Regolith on a tiny asteroid: Granular materials partly cover the surface of Itokawa (abstract #1686). 37th Lunar and Planetary Science Conference. CD-ROM.

Moroz L. V., Fisenko A. V., Semjonova L. F., Pieters C. M., and Korotaeva N. N. 1996. Optical effects of regolith processes on S-asteroids as simulated by laser shots on ordinary chondrite and other mafic materials. *Icarus* 122:366–382.

Nagao K., Okazaki R., Nakamura T., Miura Y. N., Osawa T., Bajo K., Matsuda S., Ebihara M., Ireland T. R., Kitajima F., Naraoka H., Noguchi T., Tsuchiyama A., Yurimoto H., Zolensky M. E., Uesugi M., Shirai K.,

Abe M., Yada T., Ishibashi Y., Fujimura A., Mukai T., Ueno M., Okada T., Yoshikawa M., and Kawaguchi J. 2011. Irradiation history of Itokawa regolith material deduced from noble gases in the Hayabusa samples. *Science* 33:1128–1131.

Noble S. K., Pieters C. M., Taylor L. A., Morris R. V., Allen C. C., McKay D. S., and Keller L. P. 2001. The optical properties of the finest fraction of lunar soil: Implications for space weathering. *Meteoritics & Planetary Science* 36:31–42.

Noble S. K., Keller L. P., and Christoffersen R. 2006. Chemical mapping nanometer-scale of weathered lunar space soil: New view A (abstract #1819). 37th Lunar and Planetary Science Conference. CD-ROM.

Noble S. K., Keller L. P., Christoffersen R., and Rahman Z. 2013. Variations lateral in patina lunar weathering on centimeter to scales nanometer (abstract #1298). 44th Lunar and Planetary Science Conference. CD-ROM.

Noguchi T., Nakamura T., Kimura M., Zolensky M. E., Tanaka M., Hashimoto T., Konno M., Nakato A., Ogami T., Fujimura A., Abe M., Yada T., Mukai T., Ueno M., Okada T., Shirai K., Ishibashi Y., and Okazaki R. 2011. Incipient space weathering observed on the surface of Itokawa dust particles. *Science* 333:1121–1125.

Noguchi T., Kimura M., Hashimoto T., Konno M., Nakamura T., Zolensky M. E., Okazaki R., Tanaka M., Tsuchiyama A., Nakato A., Ogami T., Ishida H., Sagae R., Tsujimoto S., Matsumoto T., Matsuno J., Fujimura A., Abe M., Yada T., Mukai T., Ueno M., Okada T., Shirai K., and Ishibashi Y. 2014. Space weathered rims found on the surfaces of the Itokawa dust particles. *Meteoritics & Planetary Science* 49:188–214.

O'Neill G. K., Billingham J., Gilbreath W., O'Leary B., and Gossett B. 1977. Space resources and space settlements. SP-NASA428. Retrieved December 8, 2003.

Papike J., Taylor L., and Simon S. 1991. Lunar minerals. In *Lunar sourcebook*, edited by Heinken G. H., Vaniman D. T. and French B. M. Cambridge, UK: Cambridge University Press. pp. 121–181.

Parman S. W., Diercks D. R., Gorman B. P., and Cooper R. F. 2015. Atom probe tomography of isoferroplatinum. *American Mineralogist* 100:852–860.

Peterman E. M., Reddy S. M., Saxey D. W., Snoeyenbos D. R., Rickard W. D. A., Fougerouse D., and Kylander-Clark A. R. C. 2016. Nanogeochronology of discordant zircon measured by atom probe microscopy of Pb-enriched dislocation loops. *Science Advances* 2. https://doi.org/10.1126/sciadv.1601318

Pieters C. M. and Noble S. K. 2016. Space weathering on airless bodies. *Journal of Geophysical Research: Planets* 121:1865–1884.

Raut U., Karnes P. L., Retherford K. D., Davis M. W., Liu Y., Gladstone G. R., Patrick E. L., Greathouse T. K., Hendrix A. R., and Mokashi P. 2018. Far-ultraviolet photometric response of apollo soil 10084. *Journal of Geophysical Research: Planets* 123:1221–1229.

Reisenfeld D. B., Wiens R. C., Barraclough B. L., Steinberg J. T., Neugebauer M., Raines J., and Zurbuchen T. H. 2013. Solar wind conditions and composition during the genesis mission as measured by in situ spacecraft. *Space Science Reviews* 175:125–164.

Rout S. S., Heck P. R., Isheim D., Stephan T., Zaluzec N. J., Miller D. J., Davis A. M., and Seidman D. N. 2017. Atom-probe tomography and transmission electron microscopy of the kamacite–taenite interface in the fast-cooled Bristol IVA iron meteorite. *Meteoritics & Planetary Science* 52:2707–2729.

Seidman D. N. and Stiller K. 2009. An atom-probe tomography primer. *MRS Bulletin* 34:717–724.

Seidman D. N., Amano J., and Wagner A. 1980. *The study of defects, radiation damage and implanted gases in solids by field ion and atom-probe microscopies.* Ithaca, New York: The Materials Science Center.

Signer P., Baur H., Derksen U., Etique P., Funk H., Horn P., and Wieler R. 1977. Helium, neon, and argon records of lunar soil evolution. Proceedings, 8th Lunar Science Conference. pp. 3657–3683.

Starukhina L. V. and Shkuratov Y. G. 2011. Iron grains reduced from nano- to micron sizes in Lunar, and Mercurian regoliths: Calculation of spectral effects (abstract #1144). 42nd Lunar and Science Conference Planetary. CD-ROM.

Stephan T., Heck P. R., Isheim D., and Lewis J. B. 2015. Correction of dead time effects in laser-induced desorption time-of-flight mass spectrometry: Applications in atom probe tomography. *International Journal of Mass Spectrometry* 379:46–51.

Taylor L. A., Pieters C. M., Keller L. P., Morris R. V., McKay D. S., Patchen A., and Wentworth S. 2001. The effects of space weathering on Apollo 17 mare soils: petrographic and chemical characterization. *Meteoritics & Planetary Science* 36:285–299.

Valley J. W., Cavosie A. J., Ushikubo T., Reinhard D. A., Lawrence D. F., Larson D. J., and Clifton P. H. 2014. Hadean age for a post-magma-ocean zircon confirmed by atom-probe tomography. *Nature Geoscience* 7:219–223.

Valley J. W., Reinhard D. A., Cavosie A. J., Ushikubo T., Lawrence D. F., Larson D. J., Kelly T. F., Snoeyenbos D. R., and Strickland A. 2015. Nano- and micro-geochronology in Hadean and Archean zircons by atom-probe tomography and SIMS: New tools for old minerals. *American Mineralogist* 1:34–42.

Wagner A. and Seidman D. N. 1979. The range profiles of 300 and 475 eV 4He+ ions and diffusivity of 4He in tungsten. *Physical Review Letters* 42:515–518.

Wieler R. 2002. Noble gases in the solar system. *Reviews in Mineralogy and Geochemistry* 47:21–70.

Wieler R., Kehm K., Meshik A. P., and Hohenberg C. M. 1996. Secular changes in the Xenon and Krypton abundances in the solar wind recorded in single lunar grains. *Nature* 384:46–49.

Zhang S. and Keller L. P. 2010. Formation of ilmenite rims in soils lunar: Deposition vapor, irradiation, and effects thermal (abstract #1432). 41st Lunar and Planetary Science Conference. CD-ROM.

Zhang S. and Keller L. P. 2011. Space weathering effects in soils lunar: Roles the of surface exposure time, and bulk chemical composition (abstract #1947). 42nd Lunar and Planetary Science Conference. CD-ROM.

Ziegler J. F., Biersack J. P., and Ziegler M. D. 2012. *SRIM: The stopping and range of ions in matter.* Morrisville, North Carolina: Lulu Press Co. http://www.srim.org

SUPPORTING INFORMATION

Additional supporting information may be found in the online version of this article.

Fig. S1. Concentration profile Tip B of H-bearing species, He, and species with a mass to charge state of 20. This concentration profile shows how these species change with depth, and the ROI does not include any of the large Fe particles. The mass-to-charge state of 20 species correlates with other oxides, and is likely dominated by Ca^+ and MgO^{++}, not Ne. The H-bearing species clearly show a higher concentration at the surface, which decreases with depth until it reaches a plateau. Unlike in Tip C, this H profile is likely dominated by H sourced from surface-adsorbed hydrogen, and from the analysis chamber and is not intrinsic to the sample. 3 ± 2 atoms of ^{4}He were detected at the same height as the vesicle, which is not included in the ROI.

Fig. S2. Concentration profiles of Fe and FeO in Tips B and C. The wide profile comes from a cylinder with a diameter of 35 nm (solid outline, upper left), and the narrow profile comes from a cylinder with a diameter of 10 nm (dotted outline, upper left). The profile presented in Fig. S1 also comes from the narrow region of interest.

Material S1. (https://www.youtube.com/watch?v=QHZhVrlooUA) An atom probe tomography (APT) reconstruction generated using IVAS. This analysis (Tip B) is from a space-weathered lunar ilmenite soil grain from sample 71501, collected by Apollo 17. This reconstruction showcases both the large microphase Fe particle (orange) surrounded by a TiO (magenta) rim, as well as a vesicle in the upper 30 nm of the tip.